

Pichel, L.M., et al., 2023, Post-salt carbonates control salt-tectonic minibasin formation:
Geology, <https://doi.org/10.1130/G51717.1>

Supplemental Material

Models SM1–SM6, Movies M1–M2, and supplemental text, figures, and equations.

Supplementary material

Why do salt tectonic minibasins form?

Leonardo M. Pichel¹, Ritske S. Huismans¹, Robert Gawthorpe¹, Jan Inge Faleide²

¹Department of Earth Science, University of Bergen, Bergen, Norway

²Department of Geosciences, University of Oslo, Oslo, Norway

Contents:

S1. Global Salt Basin Stratigraphy

S2. Numerical Methods

S3. Theoretical Quantitative Analysis

S4. Supplementary Models

References

S1 Global Salt Basin Stratigraphy

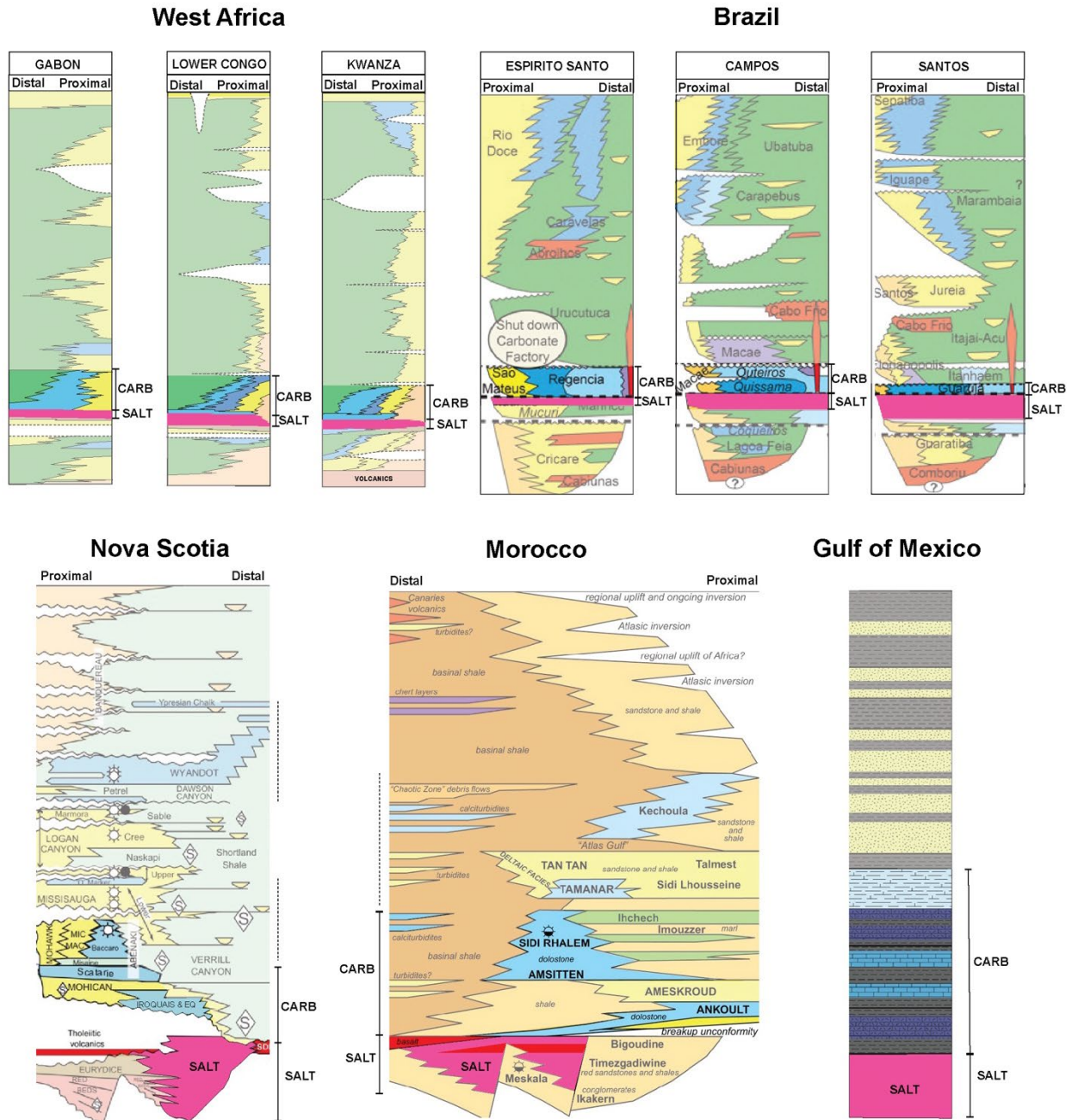


Figure S1.1: Compilation of stratigraphic columns from the largest and most well-known late syn-rift salt basins showing the presence of early and mid-late post-salt (pink) carbonates (blues) or carbonate-dominated sequences of variable thicknesses: (a) Gabon, Lower Congo and Kwanza from West Africa (adapted from Pichel et al., 2023), (b) Espírito Santo, Campos and Santos, Brazil (adapted from Beglinger et al. 2012), (c) Morocco, NW Africa (adapted from Tari and Jabbour, 2013), (d) Nova

Scotia, Canada (adapted from Deptuck and Kendal, 2017) and Gulf of Mexico, US (adapted from Dice, 2017).

S2 Numerical Methods and analysis

The model solves the force balance equations of equilibrium for quasi-static incompressible flows in two dimensions (Thieulot 2011; Theunissen and Huismans, 2019):

$$\nabla \left(\mu_{eff} (\nabla \mathbf{v} + (\nabla \mathbf{v})^T) \right) - \nabla P + \rho \mathbf{g} = 0$$

where P is the pressure, \mathbf{v} is the velocity, μ_{eff} the effective viscosity, ρ the density and \mathbf{g} the acceleration of gravity. This is coupled with time (t)-dependent heat conservation:

$$\rho c_p \frac{DT}{Dt} = \nabla(k \nabla T) + H + v_z \alpha_T g T \rho$$

where T is temperature, c_p is specific heat capacity, k thermal conductivity, and H radiogenic heat production. The last term in the heat balance equation is the temperature correction for adiabatic heating and cooling when material moves vertically at velocity v_z , where α_T represents the volumetric thermal expansion coefficient. The mechanical and thermal evolution are coupled through nonlinear temperature (T)- and pressure (P)-dependent rheologies, as well as the temperature dependence of buoyancy:

$$\rho = \rho_0 (1 - \alpha_T (T - T_0))$$

where ρ_0 is the reference density at T_0 , temperature at surface conditions, using the Boussinesq approximation, which considers that changes in density (ρ) are small enough to approximate the conservation of mass by an incompressible flow.

$$\nabla \cdot \mathbf{v} = 0$$

When the stress state is below the frictional-plastic yield stress, the flow is viscous and is defined by temperature-dependent nonlinear power law rheologies based on laboratory measurements on “wet” quartz (Gleason & Tullis, 1995) and “wet” olivine (Karato & Wu, 1993). The effective viscosity, μ_{eff} , in the power law rheology is of the general form:

$$\mu_{eff} = f A^{-1/n} \dot{E}_2^{(1-n)/2n} e^{\frac{Q+Vp}{nRT}}$$

where \dot{E}_2 is the second invariant of the deviatoric strain rate tensor $\frac{1}{2}(\dot{\epsilon}_{ij}\dot{\epsilon}_{ij})$, A is the preexponential scaling factor, n is the power law exponent, Q is the activation energy, R is the universal gas constant, and V is the activation volume. The factor f is used to scale viscosities calculated from the reference quartz and olivine flow laws, thereby producing strong and weak versions of these materials. Frictional-plastic yielding is modelled with a pressure-dependent Drucker-Prager yield criterion which is equivalent to the Coulomb yield criterion for incompressible deformation in plane strain. Yielding occurs when:

$$\sigma_y = \sqrt{J_2} = C \cos(\phi_{eff}) + P \sin(\phi_{eff})$$

where J_2 is the second invariant of the deviatoric stress, C is the cohesion, ϕ_{eff} is the effective internal angle of friction following $P \cdot \sin(\phi_{eff}) = (P - P_f) \sin(\phi)$ and P_f is the pore fluid pressure. This yield criterion approximates frictional sliding in rocks, including pore-fluid pressure effects. Frictional-plastic strain softening is introduced by a linear decrease of $\phi_{eff}(\epsilon)$ from 15° to 2° and $C(\epsilon)$ from 20 to 4 MPa with respect to plastic strain (ϵ); Buck, 1993; Huisman & Beaumont, 2002; Lavier et al., 1999, 2000). The plastic strain is updated at every time-step with the second invariant of the deviatoric strain. The incompressible plastic flow becomes equivalent to a viscous flow if an effective viscosity, μ_{eff}^p , for a plastic material is defined such that $\mu_{eff}^p = \frac{\sqrt{J_2}}{\sqrt{\dot{E}_2}}$. Setting the viscosity to μ_{eff}^p in regions that are on frictional-plastic yield satisfies the yield

condition and allows the velocity field to be determined from the finite element solution of equation (1). The overall nonlinear solution is determined iteratively using $\mu = \mu_{eff}^p$ (for regions of plastic flow) and $\mu = \mu_{eff}^v$ (for regions of viscous flow; Willett, 1992).

Model Initial Configuration

The models are designed as an idealized rheologically layered lithosphere above a sublithospheric mantle in a 600-km-high and 1,200-km-wide model domain (Figure A2). The lithosphere consists of a 35-km-thick crust and 85-km mantle lithosphere overlying sublithospheric mantle. The uppermost 3 km of the crust represents pre-rift sediments with the same rheology as the upper crust. The Eulerian grid consists of 2,400 and 290 elements in the horizontal and vertical directions, respectively. The distribution of the elements is irregular in the vertical direction, allowing for high resolution in the upper crust with a vertical resolution of $\Delta z = 200$ m in the first 20 km, $\Delta z = 625$ m between 20 and 70 km, $\Delta z = 1,100$ m between 70 and 120 km, and $\Delta z = 7,917$ m between 120 and 600 km. The resolution in the horizontal direction is 500 m for the entire model domain. Extensional horizontal velocity boundary conditions ($v = \pm 0.5$ cm/year) are applied to the lithosphere, and the corresponding exit flux is balanced by a low velocity inflow in the sublithospheric mantle. The top of the model is a free surface. The sides and base are vertical and horizontal free slip boundaries, respectively (Figure S2.1). All values used for the mechanical and thermal parameters are listed in Table S2.2

Thermal boundary conditions are specified basal temperature, 1,520 °C, and insulated lateral boundaries. The initial temperature field is laterally uniform and increases with depth from the surface ($T_0 = 0$ °C) to the base of the crust (initial Moho temperature, $T_m = 550$ °C) with a surface heat flux of 55.3 mW/m². Below the Moho, temperature linearly increases to the base of mantle lithosphere (initially at $T = 1,328$ °C); the temperature of the sublithospheric mantle follows an

adiabatic gradient ($0.4\text{ }^{\circ}\text{C}/\text{km}$). Thermal conductivity linearly increases to $51.46\text{ W}\cdot\text{m}^{-1}\cdot\text{K}^{-1}$ at $1,350\text{ }^{\circ}\text{C}$ ($\sim 125\text{-km}$ depth), corresponding to scaling the thermal conductivity by the Nusselt number of upper mantle convection. The enhanced conductivity maintains a nearly constant heat flux to the base of the lithosphere and an adiabatic temperature gradient in the sublithospheric mantle (e.g., Pysklywec & Beaumont, 2004).

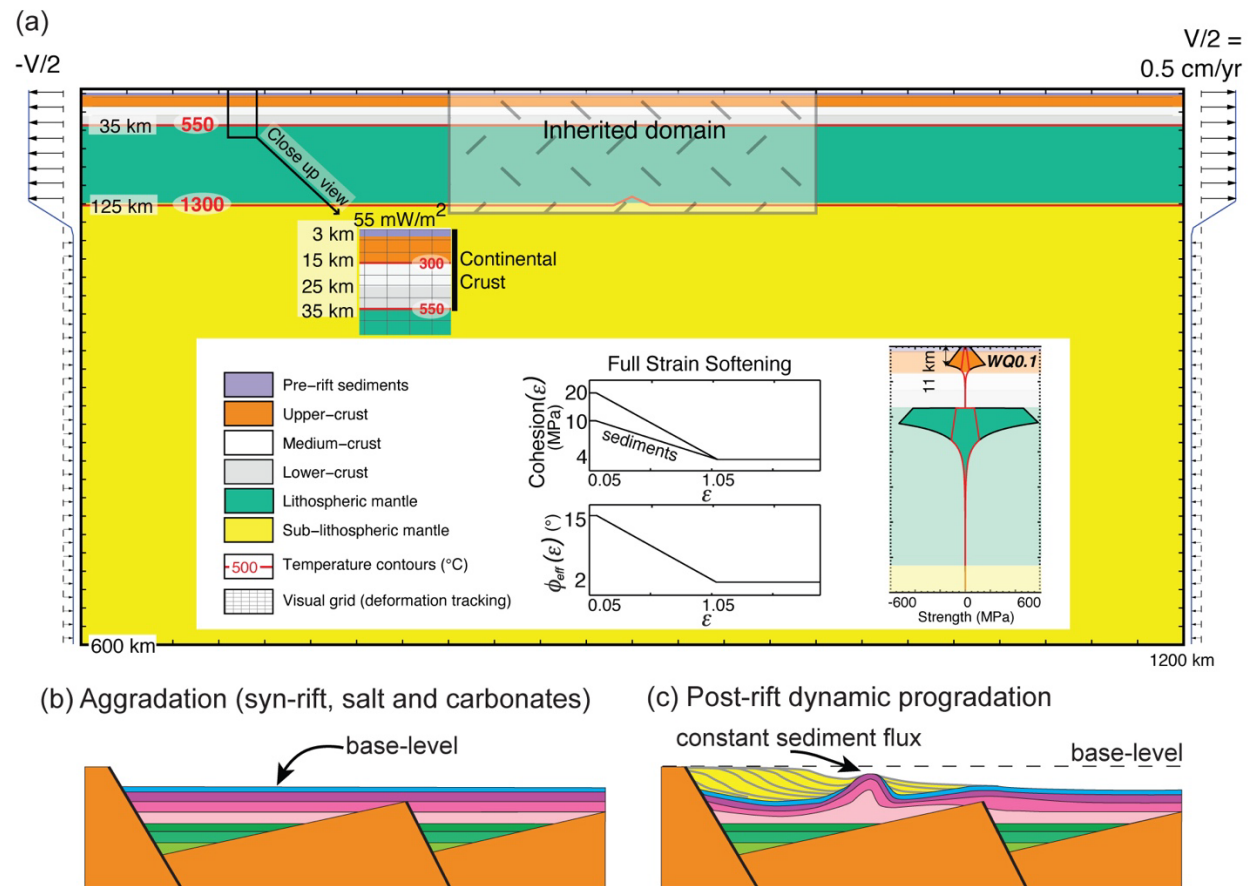


Figure S2.1: (a) Model setup showing rheological-layered structure, boundary conditions, initial thermal state, and frictional-plastic strain softening conditions. The values used for the mechanical and thermal parameters are listed in Table S2.2. (b) Schematic diagram illustrating syn-rift aggradation for syn-rift sediments (greenish colors), salt (pink-magenta) and post-salt carbonates (blue) in which sediments aggrade towards local basement lows. (c) Schematic diagram illustrating post-rift (post-salt) dynamic progradation (yellow) in which the depositional profile changes in shape and length through time according to the evolving salt topography.

We follow the same approach of Theunissen and Huismans (2019) and apply a white noise in the initial strain field (Figure S2.1) that represents mechanical heterogeneity and inheritance of deformation from previous tectonic phases. Specifically, the plastic strain (ϵ) is initialized with white noise that has a Gaussian distribution with a mean value set to 0.3 and with a maximum value 0.8. Inherited weakness is provided by a tapered symmetrical 400-km-wide area in the model center. A minor thermal heterogeneity is introduced at the base of the lithosphere in the model center in order to enhance rift localization so that the orientation of faults and rift geometries are not prescribed and are generated spontaneously (Fig. S2.1). To ensure mass conservation, the average pressure at the bottom part of the model is maintained constant by adjusting the influx of the sublithospheric mantle at the sides of the model. This allows defining an absolute sea level within the model independent from the surface displacement. A water load is implemented based on the defined sea-level to guarantee that all mass loads on the free surface are modelled.

Parameter	Symbol	Units	Salt	Clastics	Carbonates	Upper crust (0-25 km)	Lower crust (25–35 km)	Lithospheric mantle	Sub- lithospheric mantle
Rheological parameters									
Effective viscosity range	μ_{eff}	Pa.s	10^{19} , 10^{18} , $5 \cdot 10^{18}$	10^{18} – 10^{27}		10^{18} – 10^{27}	10^{18} – 10^{27}	10^{18} – 10^{27}	10^{18} – 10^{27}
Angle of internal friction	ϕ_{eff}	—	-	15		15		15	
→ after strain weakening	ϕ_{eff}	—	-	2		2		4	
Initial cohesion	C	MPa	-	10	10, 20	20		20	
→ after strain weakening	C	MPa	-	4		4		20	
Strain weakening range	—	—	-	0.05–1.05					
Flow law	—	—	-	WQtz ^a				WO ^b	
Scaling factor	f_c	—	-	1		0.1		5	1
Power law exponent	n	—	-	4		4		3	
Activation energy	Q	kJ/mol	-	222.81		222.81		429.83	
Constant	A	Pa ^{-n} /s	-	8.574×10^{-28}				1.758×10^{-14}	
Activation volume	V	m ³ /mol	-	0.0				15×10^{-6}	
Density at T ₀ = 273 K	ρ_0	kg/m ³	2200	see text	2400	2750	2900	3300	
Thermal parameters									
Thermal conductivity	k	W/m/K	2.25					2.25-5.6	
								2.25–51.46	
Heat capacity	c_p	J/K/kg	803.57			818.18	775.86	681.81	
Thermal diffusivity	κ	m ² /s	1.0×10^{-6}					1 - 2.5×10^{-6}	
								$1 - 22.87 \times 10^{-6}$	
Heat production rate	H	W/m	0.8×10^{-6}			1.12×10^{-6}	0.48×10^{-6}	0	
Thermal expansion	α_T	1/K	3×10^{-5}	3.1×10^{-5}					
Boundary conditions									
Surface temperature	T_{surf}	°C				0			
Pre-rift sediment thickness	$h_{pre-sed}$	km				3			
Initial Moho depth	d_{moho}	km				35			
Moho Temperature	T_{moho}	°C				550			
LAB depth	d_{LAB}	km				125			
LAB temperature	T_{LAB}	°C				1328			
Basal temperature	T_{LM}	°C				1520			
Extension velocity	V_{ext}	cm/year				1			

Table S2.1: Parameters for the Lithosphere-Scale Thermo-Mechanical Models of salt-bearing wide rifted margins. Flow laws are based on power law with creep parameters from wet quartz (Gleason & Tullis, 1995) and wet olivine (Karato & Wu, 1993). Values are given with two digits precision. WQtz = wet quartz; WO = wet olivine; LAB = Lithosphere-Astenosphere Boundary. ^aDislocation creep models for WQtz. ^bDislocation creep models for WO. Parameters in bold-italic correspond to supplementary models.

Sedimentation

For the aggradation approach, the area of sediment deposition is maintained constant over an infinitesimal length of the model so that the sediment thickness varies according to the evolving rift topography. This results in a more realistic scenario where deep and/or narrow grabens will present thicker strata than wide and/or shallow grabens (Fig. S2.1).

For the dynamic progradation, deposition is controlled by specifying a constant sediment flux, Q_s to the basin that is based on a characteristic sediment transport length L_d and sediment flux Q_s following:

$$d_{offshore} = Q_s \frac{dx}{L_d}$$

where $d_{offshore}$ is the sediment discharge per unit width (e.g., Theunissen and Huismans, 2019).

S3. Theoretical Quantitative Analysis

We compute the average density of the post-salt sediments including the carbonates and compacting clastics as a function of the thickness of the carbonate layer and of clastic sediment accumulation, and water load. Clastics have an initial grain density (ρ_g) of 2650 kg m⁻³, surface porosity (n_0) of 0.52 and compact with depth (z) following:

$$\rho(z) = \rho_g - (\rho_g - \rho_w)n_0e^{-cz}$$

Where ρ is the bulk (average weighted) density of sediments as a function of depth, water content and ρ_w water (pore fluid) density (1000 kg m⁻³), and c is the compaction coefficient of 4.7 x 10⁻⁴ m⁻¹ (Atty 1930; Jackson and Talbot, 1986; and Goteti et al., 2012). The carbonates have a density of 2400 kg m⁻³, salt of 2200 kg m⁻³ and do not compact. Water density is of 1000 kg m⁻³. Average minibasin density can be obtained by integrating $n(z) = n_0e^{-cz}$ over the thickness of the clastic succession in the minibasin (e.g., Goteti et al., 2012):

$$\rho_{avg}(h_{mb}) = \rho_g + \frac{(\rho_g - \rho_w)n_0}{c \times h_{mb}} * (e^{-c \cdot h_{mb}} - 1)$$

We consider that water loading leads to an initial compaction at the top of the minibasin controlled by the equivalent water depth which is given by:

$$h_{w_eq} = h_w * \rho_w / \rho_{s_average}$$

Where h_w is water-depth and h_{w_eq} is the equivalent burial depth at the surface of the minibasin by water loading that can be interpreted as the burial depth by a rock column with average sediment density given by $\rho_{s_average} = (\rho(0) + \rho_g)/2$. Average post-salt sediment clastic density including initial compaction by water loading is consequently given by:

$$\rho_{avg}(h_{mb}) = \rho_g + \frac{(\rho_g - \rho_w)n_0}{c \times h_{mb}} * (e^{-c*(h_{mb}+h_{w_eq})} - e^{-c*h_{w_eq}})$$

Where h_{mb} is the thickness (height) of the clastic compacting sequence in the minibasin. Average minibasin density, including carbonates and clastic is consequently:

$$\rho_{mb_avg}(h_{mb}, h_c) = \frac{\rho_c * h_c + \rho_{avg} * h_{mb}}{h_c + h_{mb}}$$

where h_c is the thickness of the carbonate layer.

S4. Supplementary Models

S4.1 Variable salt viscosity

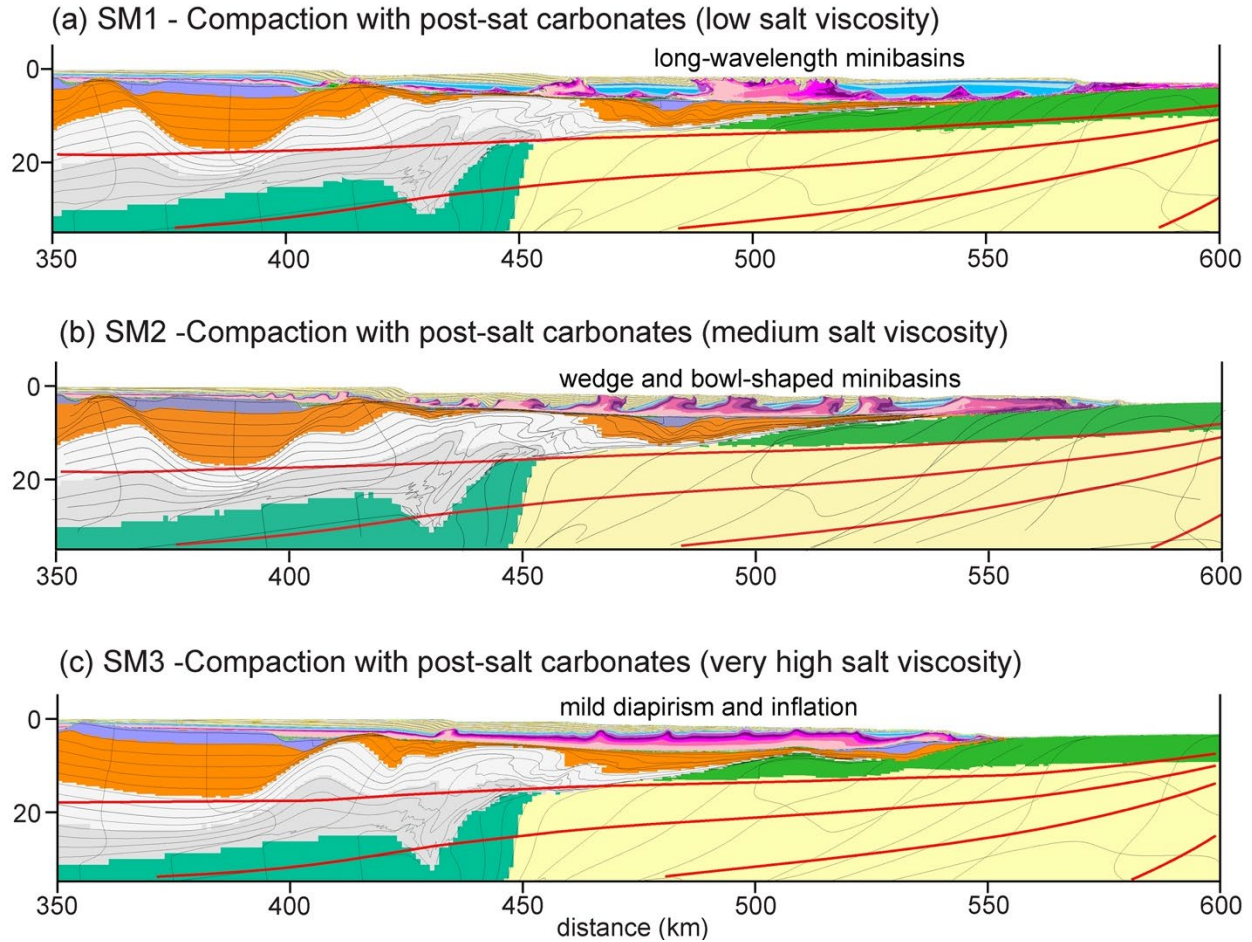


Figure S4.1: Model Set with variable salt viscosities: (a) SM1 - model with low salt viscosity (10^{18} Pa s) and post-salt carbonates and followed by clastic progradation showing very wide minibasins (three minibasins with ~ 22 km of average width). Minibasins form fast, during the earliest stages of post-salt sediment deposition due to the very efficient low-viscosity salt flow and differential sediment loading by post-salt carbonates. (b) SM2 - model with intermediate salt viscosity (5×10^{18} Pa s) and post-salt carbonates followed by clastic progradation showing six wedge- and bowl-shaped minibasins with an average of 9.6 km of width. (c) SM3 – model with very high (5×10^{19} Pa s) and post-salt carbonates followed by clastic progradation showing no typical minibasin geometry, apart from very subtle depocentres, and mild diapirism, distal salt inflation and folding.

S4.2 High post-salt carbonate cohesion

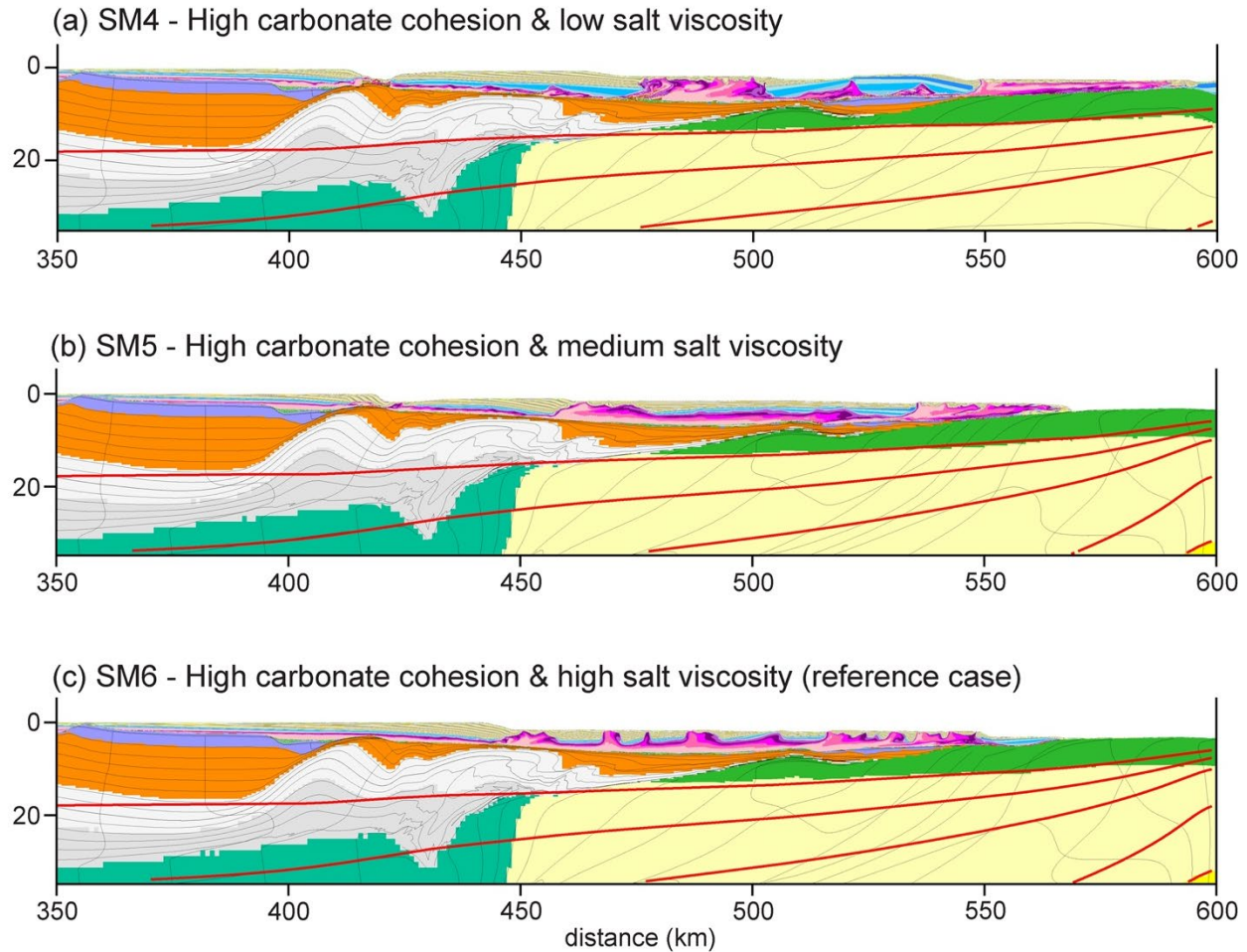


Figure S4.1: Model Set testing the role of higher post-salt carbonate cohesion ($C = 20$ MPa) for different salt viscosities: low (10^{18} Pa s), medium (5×10^{18} Pa s), and high (10^{19} Pa s). (a) SM4 with low salt viscosity, (b) SM5 with intermediate salt viscosity and (c) SM6 with high salt viscosity. Note that increasing cohesion results in generally fewer, simpler, and wider minibasins for all salt viscosities (compare with reference model M1 and SM1-2).

References

- Beglinger, S. E., Doust, H., and Cloetingh, S. A. P. L, 2012. Relating petroleum system and play development to basin evolution: Brazilian South Atlantic margin. *Petroleum Geoscience* 18(3), 315–336.
- Buck, W. R., 1993. Effect of lithospheric thickness on the formation of high- and low-angle

- normal faults. *Geology*, 21(10), 933–936.
- Deptuck, M. E., and Kendell, K. L., 2017. A review of Mesozoic-Cenozoic salt tectonics along the Scotian margin, eastern Canada. *Permo-triassic salt provinces of Europe, north Africa and the Atlantic margins*, 287-312.
- Gleason, G. C., and Tullis, J., 1995. A flow law for dislocation creep of quartz aggregates determined with the molten salt cell. *Tectonophysics*, 247(1–4), 1–23. (30 Years of Tectonophysics a Special Volume in Honour of Gerhard Oertel).
- Huismans, R. S., & Beaumont, C., 2002. Asymmetric lithospheric extension: The role of frictional plastic strain softening inferred from numerical experiments. *Geology*, 30(3), 211–214.
- Karato, S.-I., & Wu, P., 1993. Rheology of the upper mantle: A synthesis. *Science*, 260(5109), 771–778.
- Lavier, L., Roger Buck, W., and Poliakov, A. N. B., 1999. Self-consistent rolling-hinge model for the evolution of large-offset low-angle normal faults. *Geology*, 27(12), 1127–1130.
- Lavier, L., Buck, W. R., and Poliakov, A. N. B., 2000. Factors controlling normal fault offset in an ideal brittle layer. *Journal of Geophysical Research*, 105(B10), 23,431–23,442.
- Pichel, L. M., Legeay, E., Ringenbach, J-C., Callot, J-P., 2023. The salt-bearing rifted margins in West Africa – regional structural variability and salt tectonics between Gabon and Namibe. *Basin Research* (*in press*)
- Theunissen, T., and Huismans, R. S., 2019. Long-term coupling and feedback between tectonics and surface processes during non-volcanic rifted margin formation. *Journal of Geophysical Research: Solid Earth*, 124(11), 12323-12347
- Tari, G., and Jabour, H., 2013. Salt tectonics along the Atlantic margin of Morocco. *Geological*

Society, London, Special Publications, 369(1), 337-353.

Thieulot, C., 2011. Fantom: Two- and three-dimensional numerical modelling of creeping flows for the solution of geological problems. *Physics of the Earth and Planetary Interiors*, 188(1–2), 47–68. <http://doi.org/10.1016/j.pepi.2011.06.011>

Willett, S. D., 1992. Dynamic and kinematic growth and change of a Coulomb wedge. In McClay, K. R. (Ed.), *Thrust tectonics*. Dordrecht: Springer Netherlands, pp. 19–31. <https://doi.org/10.1007/978-94-011-3066-0>.